Supplementary Information

Surfactant enhanced $Cu^{\delta+}$ and induced electrostatic force promoted dechlorination for deuteroacetic acid electrosynthesis with D_2O

Qin et al.

Table of contents

Supplementary Figures 1–46

(Including NMR, HR–MS, and GC–MS data)

Supplementary Notes 1–22

Supplementary References 1–20

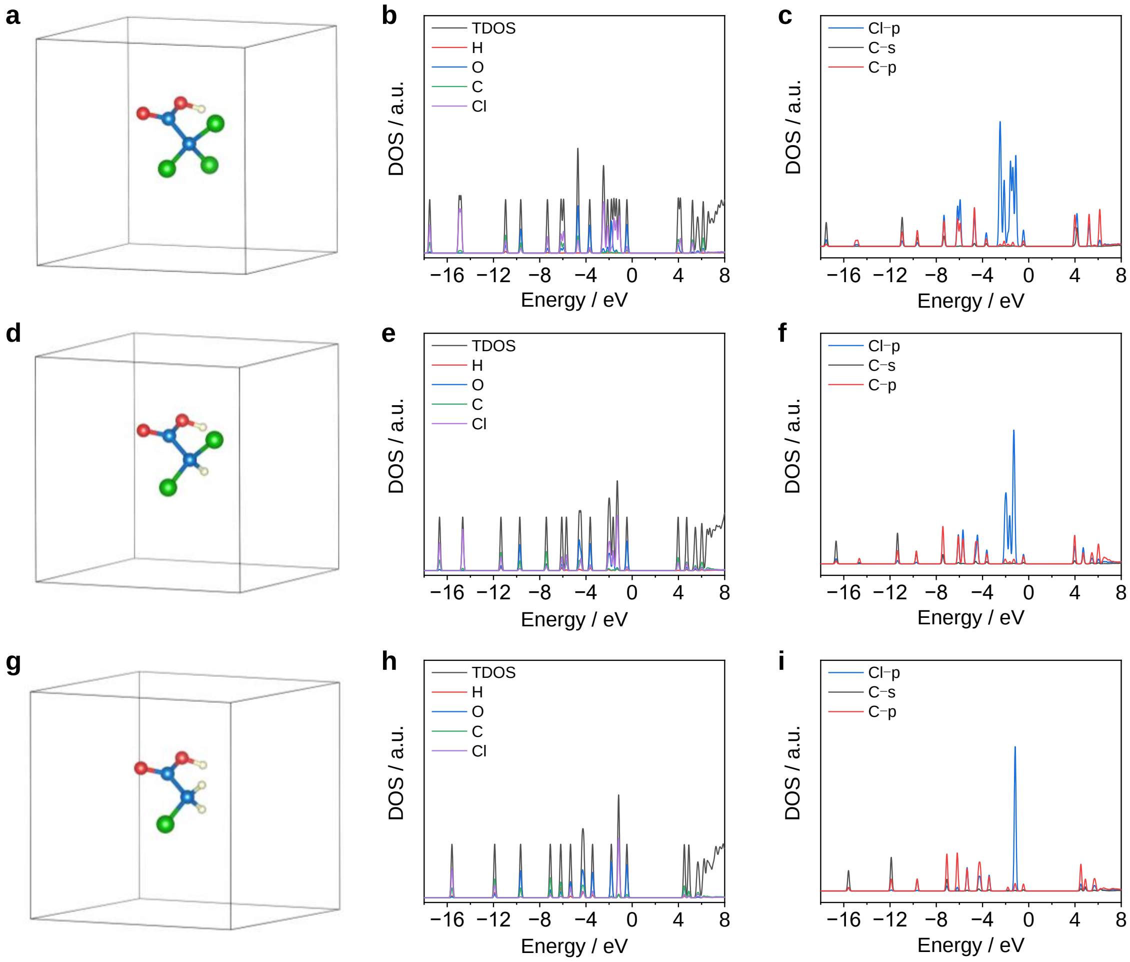

Supplementary Fig. 1 Partial density of states (PDOS) analysis. Partial density of states (PDOS) analysis. Structural diagram of **a,** TCAA; **d,** DCAA; **g,** MCAA. PDOS of H, C, O, and Cl atoms in **b,** TCAA, **e,** DCAA, **h,** MCAA. PDOS of Cl p-orbitals, C s-orbitals and C p-orbitals in **c,** TCAA, **f,** DCAA, **i,** MCAA. The Fermi level is set to 0 eV.

Supplementary note 1 From the obtained PDOS plots, the C−Cl interactions in the TCAA, DCAA, and MCAA molecules are notably different,[1] suggesting that the dissociation of the C−Cl bond may become increasingly difficult as the Cl atoms are gradually removed in the electroreduction of TCAA.

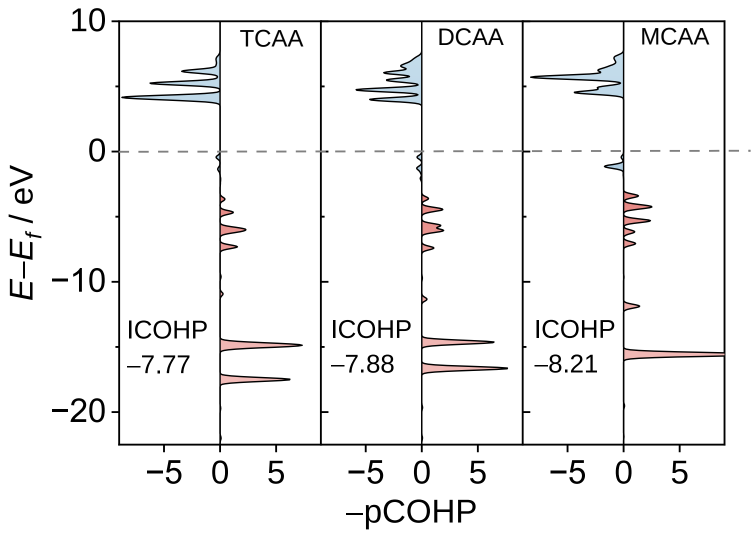

Supplementary Fig. 2 Projected crystal orbital Hamilton population (pCOHP) analysis. Projected crystal orbital Hamilton population (pCOHP) analysis. −pCOHP for the C−Cl interaction of TCAA, DCAA, and MCAA. The blue and red regions represent antibonding and bonding states, respectively. The dashed line represents the Fermi level.

Supplementary Note 2 In contrast to those of TCAA and DCAA, the antibonding state of the C−Cl interaction in MCAA moves up to E_f.[2–3] The integrated COHP (ICOHP) values of TCAA, DCAA, and MCAA obtained by integrating the energy up to E_f are calculated as −7.77, −7.88, and −8.21, respectively. A more negative ICOHP means a stronger C−Cl interaction, which indicates that the dissociation of the C−Cl bond in MCAA has a greater energy barrier.

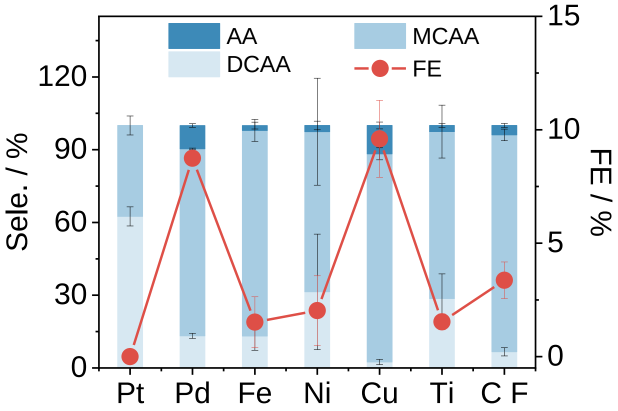

Supplementary Fig. 3 The product distributions and FEs over different cathode electrodes. Reaction conditions: 0.5 mmol TCAA in 0.5 M K_2CO_3 with a passed charge of 300 C at −100 mA cm^{-2}. The error bars correspond to the standard deviation of at least three independent measurements.

Supplementary Note 3 Seven common cathodic electrode materials, namely, Pt, Pd, Fe, Ni, Cu, Ti, and CF (carbon fibre), were tested to investigate their performance in the electroreduction of TCAA to AA. The Cu electrode exhibited the highest AA selectivity. Thus, Cu was chosen for modification to improve the reaction performance.

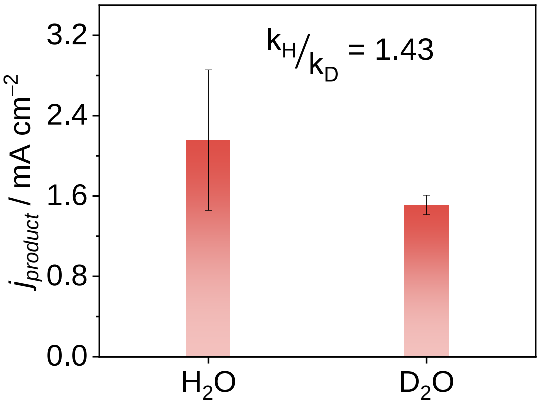

Supplementary Fig. 4 Kinetic isotope effect (KIE) experiments over the CS-Cu cathode. Conditions: 0.5 mmol TCAA in 0.5 M K_2CO_3 by using H_2O and D_2O as electrolytes at –0.75 V vs. Hg/HgO with a passed charge of 28.95 C. All the potentials in this work were referred to as Hg/HgO unless otherwise stated.

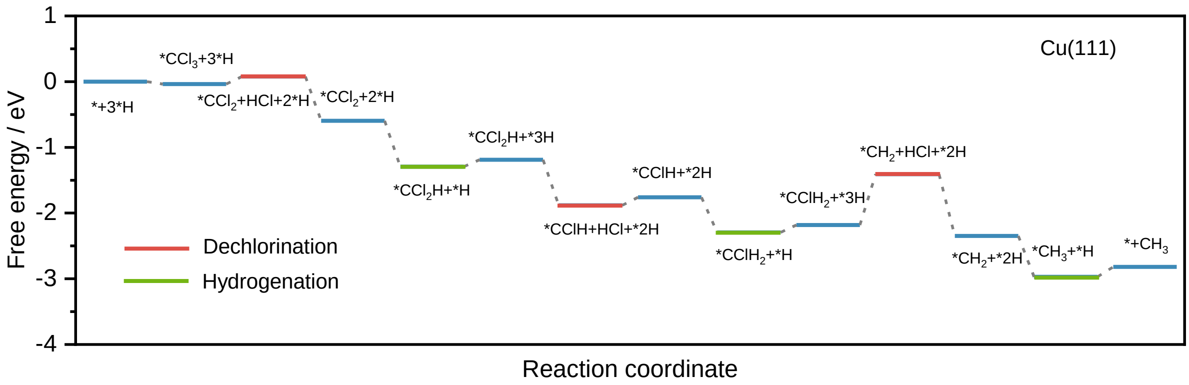

Supplementary Fig. 5 Gibbs free energy diagram for the dechlorination of TCAA on Cu(111) at 0 V vs. RHE. To simplify, the carboxyl group is omitted. Asterisks represent the adsorption state of the active species.

Supplementary Note 4 In the process of TCAA electroreduction, the removal of Cl atoms occurs through a stepwise process. TCAA first overcomes an uphill energy of 0.12 eV to remove the first Cl atom, and the energy for removing the second Cl atom is –0.69 eV, indicating an exothermic process. The removal of the last Cl atom requires an uphill energy of 0.77 eV, suggesting the difficulty of activating the C–Cl bond in MCAA.

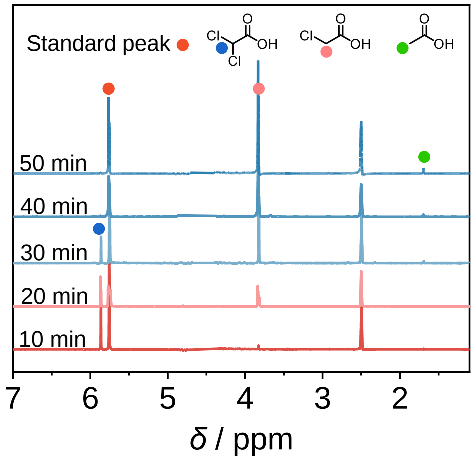

Supplementary Fig. 6 ^{1}H NMR detection. In situ time-dependent ^{1}H NMR spectra of the TCAA electroreduction process on CS-Cu at −100 mA cm^{-2}.

Supplementary Note 5 During the electroreduction of TCAA, the main product within the first 10 minutes is DCAA, which gradually converts to MCAA in 10–40 minutes. The MCAA gradually converts to AA in the last 10 minutes. Notably, the selectivity of AA for CS-Cu is low.

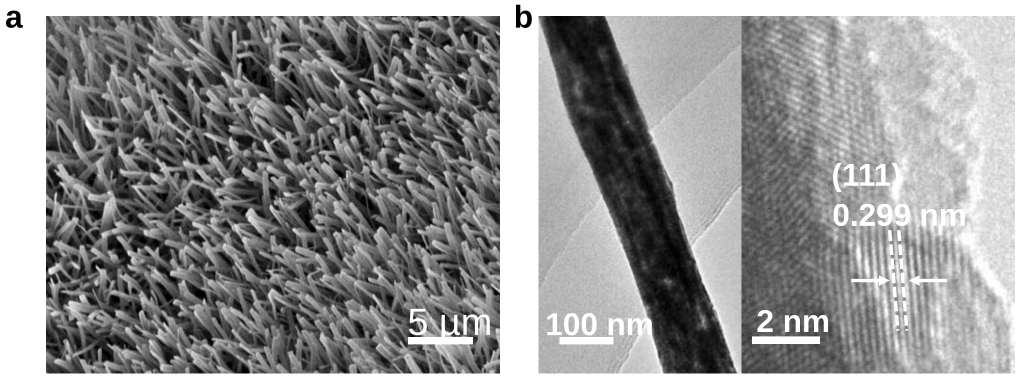

Supplementary Fig. 7 Morphology characterizations. SEM (**a**) and TEM (**b**) images of the LC–Cu nanorods.

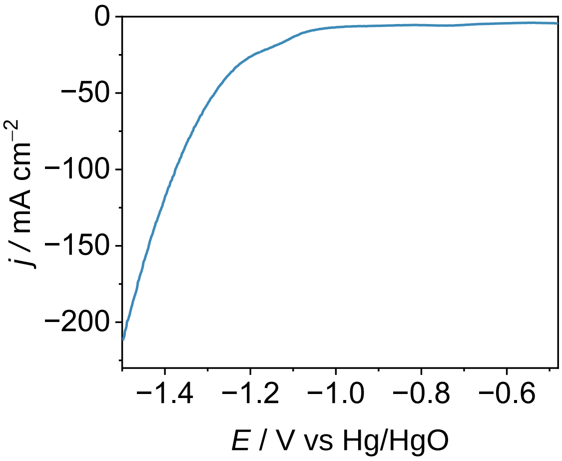

Supplementary Fig. 8 LSV curve. LSV curve of LC-Cu at a scan rate of 10 mV s^{-1} in 0.5 M K_2CO_3 solution.

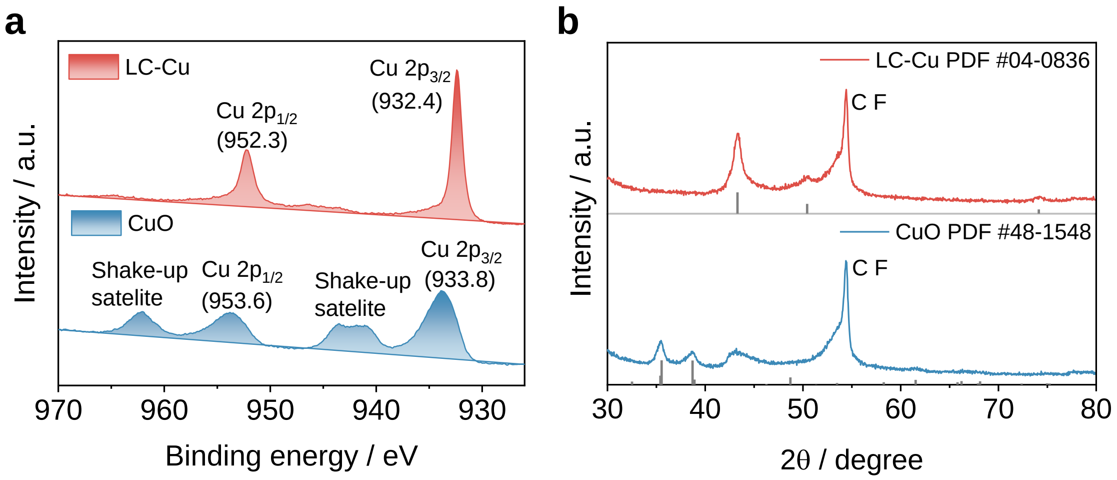

Supplementary Fig. 9 Characterization of CuO and LC-Cu. a, Cu 2p XPS spectra of CuO and LC-Cu. **b**, XRD patterns of CuO and LC-Cu.

Supplementary Note 6 In the Cu 2p XPS spectra, the two peaks located at 932.4 eV and 952.3 eV belong to Cu(0) $2p_{3/2}$ and Cu(0) $2p_{1/2}$, respectively, demonstrating the formation of metallic Cu. To eliminate the background signal influence from the Cu substrate, CF was used as the substrate for XRD test. The XRD peaks at 43.3°, 54.4°, and 74.1° were indexed to the (111), (200), and (220) planes of Cu(0) (PDF #04-0836), which also verified the formation of LC-Cu.

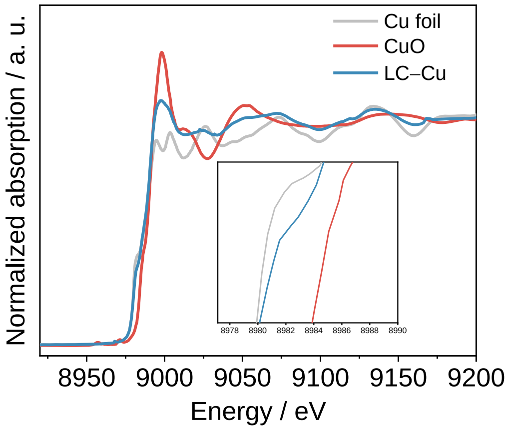

Supplementary Fig. 10 XANES characterization of LC-Cu. The spectra of the Cu foil and CuO are shown for comparison.

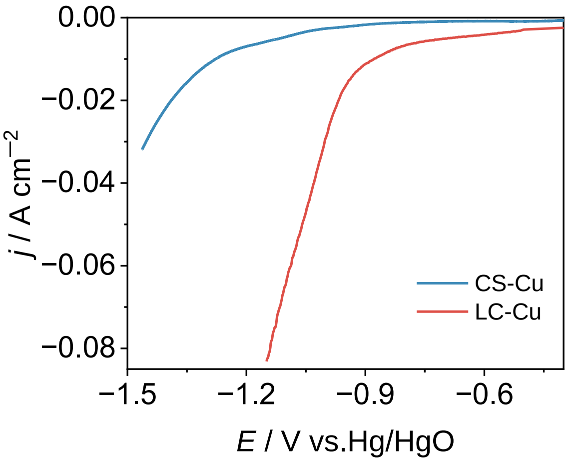

Supplementary Fig. 11 LSV curves of MCAA-*d*$_3$ on CS-Cu and LC-Cu.

Supplementary Note 7 Compared with CS-Cu, MCAA-*d*$_3$ shows a significant overpotential reduction on LC-Cu, suggesting that LC-Cu can effectively enhance the deuteriation of MCAA-*d*$_3$.

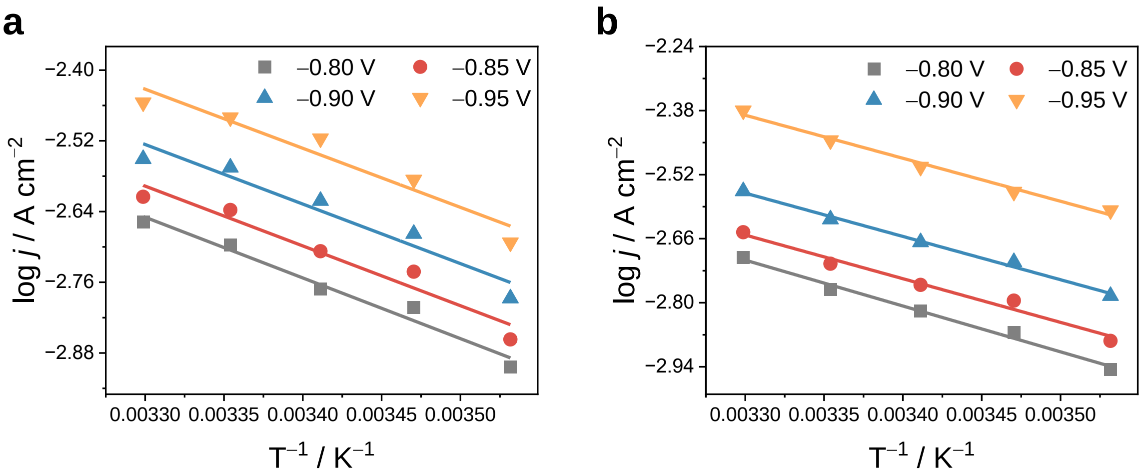

Supplementary Fig. 12 Activation energy detection. Arrhenius plots of the current at different potentials over **a,** CS-Cu and **b,** LC-Cu with MCAA-d_3 as the substrate. We transfer the LC-Cu onto carbon fibre, the same substrate as CS-Cu to ensure an accurate comparison in the activation energy detection.

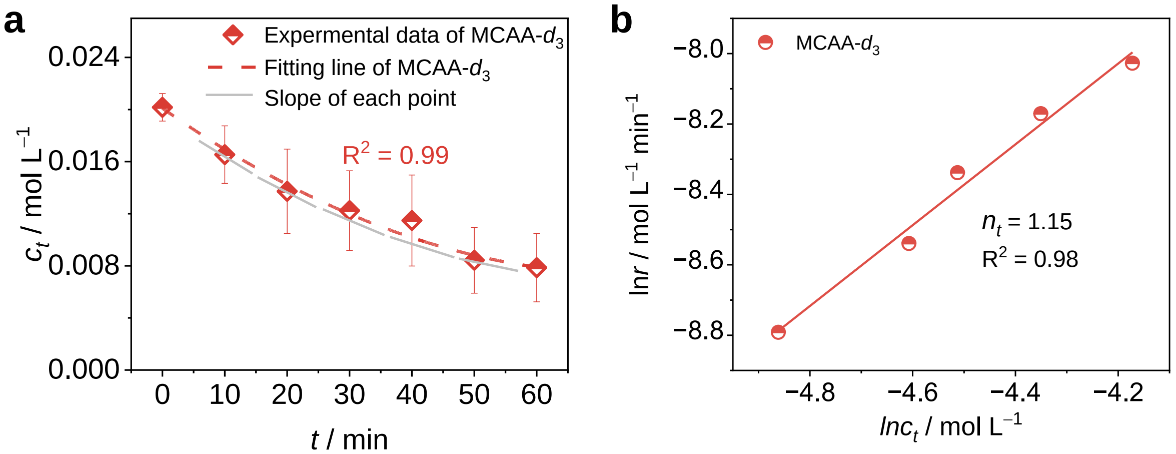

Supplementary Fig. 13 Reaction rate detection. **a**, Time-dependent residual concentration c_t of the MCAA-d_3 curve at –0.95 V. **b**, Experimentally measured order of reaction, n_t, of MCAA-d_3 on LC-Cu.

Supplementary Note 8 The $c_t \sim t$ curve is obtained by measuring the residual concentration of MCAA-d_3 at various time points. The Gaussian fitting equation for the $c_t \sim t$ curve is given by: $y = 0.020 - 3.70 \times 10^{-4} x + 2.18 \times 10^{-6} x^2$. The derivative of the fitting equation is used to obtain the slope r at each point (grey line). Then, plotting lnr against lnc gives the reaction order n_t. The n_t value of 1.15 indicates that the deuteriation of MCAA-d_3 follows a first-order kinetic model.

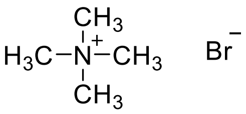

Tetramethylammonium bromide (TMAB)

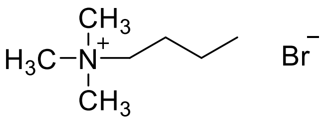

Butyltrimethylammonium bromide (BTAB)

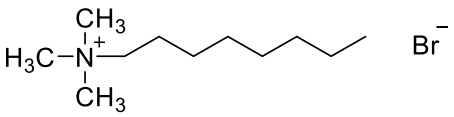

Octyltrimethylammonium bromide (OTAB)

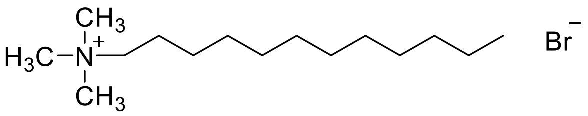

Dodecyltrimethylammonium bromide (DTAB)

Supplementary Fig. 14 Structures of four different quaternary ammonium surfactants.

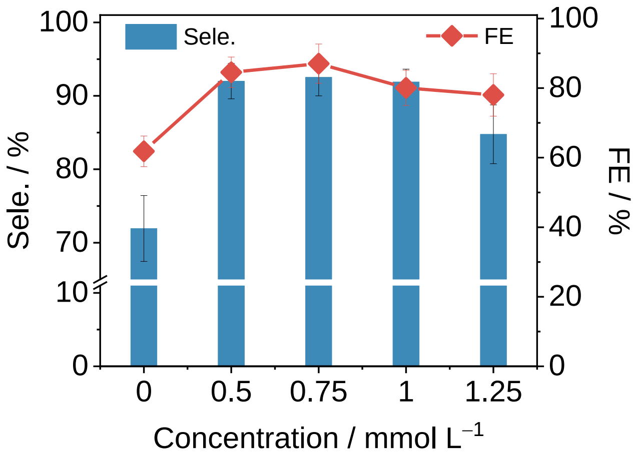

Supplementary Fig. 15 Reaction performance. Seles. and FEs of AA with various concentrations of OTAB at –100 mA cm^{-2} with a passed charge of 300 C.

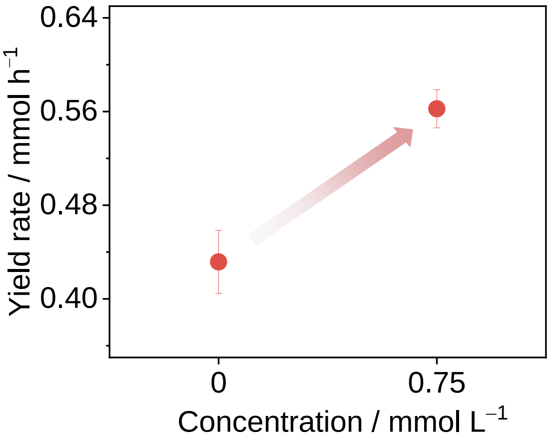

Supplementary Fig. 16 The yield rates of AA on LC-Cu without and with 0.75 mM OTAB. Conditions: 0.5 mmol TCAA in 0.5 M K_2CO_3 solution at –100 mA cm^{-2} with a passed charge of 300 C.

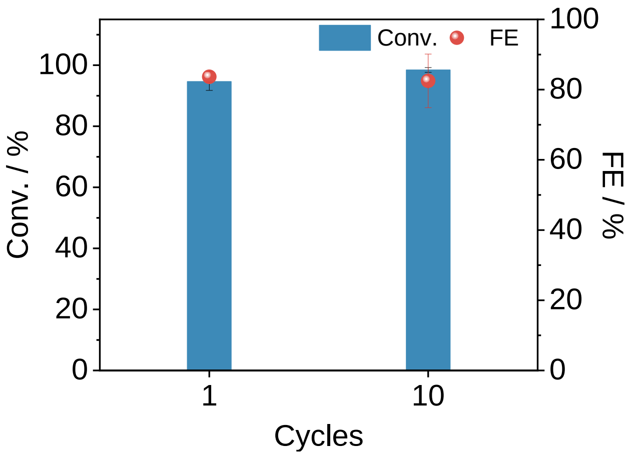

Supplementary Fig. 17 Cycle-dependent TCAA conv. and FEs of AA over LC-Cu. Conditions: 0.5 mmol TCAA and 0.75 mM OTAB in 0.5 M K_2CO_3 solution at −100 mA cm^{-2} with a passed charge of 240 C per cycle.

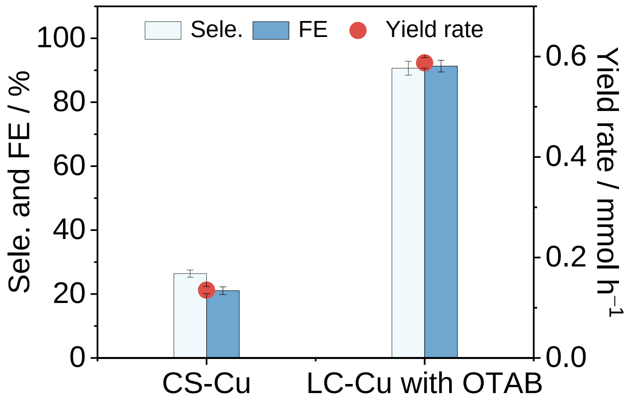

Supplementary Fig. 18 The Seles. and FEs of AA-*d*$_4$ on CS-Cu without and LC-Cu with 0.75 mM OTAB. Conditions: 0.5 mmol TCAA in 0.5 M K_2CO_3 D_2O solution at −100 mA cm^{-2} with a passed charge of 300 C.

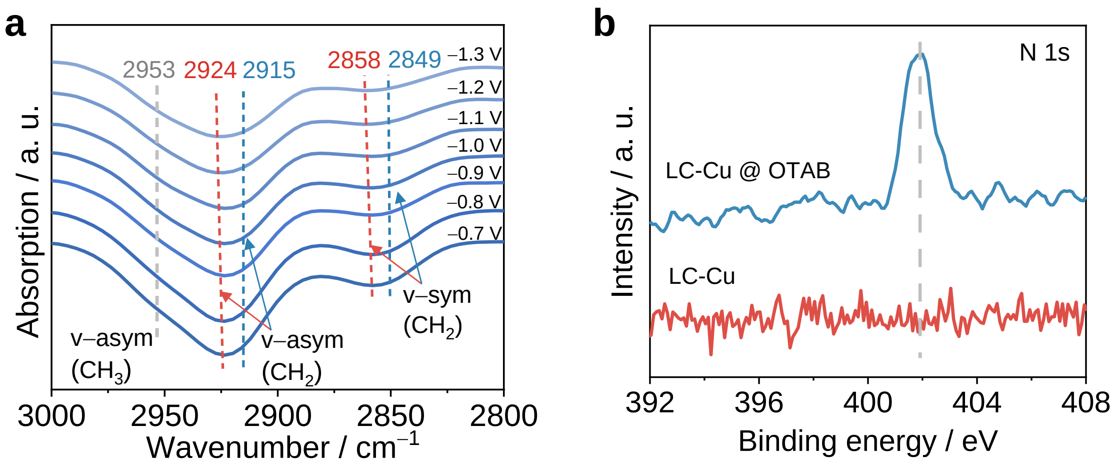

Supplementary Fig. 19 Investigation of OTAB adsorption behaviour. a, Potential-dependent in situ ATR-FTIR spectra under various potentials for the OTAB-introduced system and **b,** N 1s XPS spectra of the OTAB–introduced system before and after bias.

Supplementary Note 9 As shown in supplementary Fig. 19a, the band centred at 2953 cm^{-1} is assigned to the symmetric C–H stretching vibrations of CH_3 in the head group (N–CH_3) of OTAB. The asymmetric and symmetric stretching vibrations of C–H of CH_2 near the head groups (2924 cm^{-1} and 2858 cm^{-1}) and the tail groups (2915 cm^{-1} and 2849 cm^{-1}) are observed. The vibrations of the C–H bonds of CH_2 near the head group gradually blueshifted, and those of the tail groups redshifted with increasing bias potential, indicating the adsorption of OTAB on the LC-Cu surface and the formation of an ordered arrangement, with the head group on the electrode surface and the tail alkyl chain group reaching the electrolyte. The N 1s XPS spectrum of LC-Cu after electrolysis shows a peak at 401.9 eV, which is attributed to the –R_4N^+ of OTAB, further indicating the adsorption of OTAB on the LC-Cu electrode (Supplementary Fig. 19b).

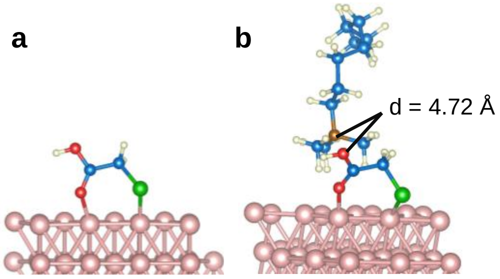

Supplementary Fig. 20 Adsorption configuration simulation. Theoretical models of MCAA intermediate adsorption on LC-Cu **a,** without OTAB and **b,** with OTAB.

Supplementary Note 10 The distance (*d*) between N^+ in OTAB and O^- in MCAA is simulated as 4.72 Å, indicating the nonnegligible existence of electrostatic force.[4–5]

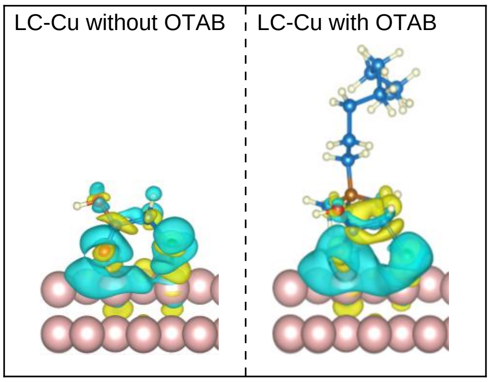

Supplementary Fig. 21 Charge density difference for *MCAA on LC-Cu without OTAB and with OTAB (0.001 e Å^{-3}). The blue and yellow isosurfaces correspond to electron deletion and accumulation, respectively.

Supplementary Note 11 Increased electron transfer occurs between LC-Cu and MCAA in the presence of OTAB,[6–7] indicating that the addition of OTAB enhances the adsorption of MCAA-d_3, thus facilitating the electron transfer process.

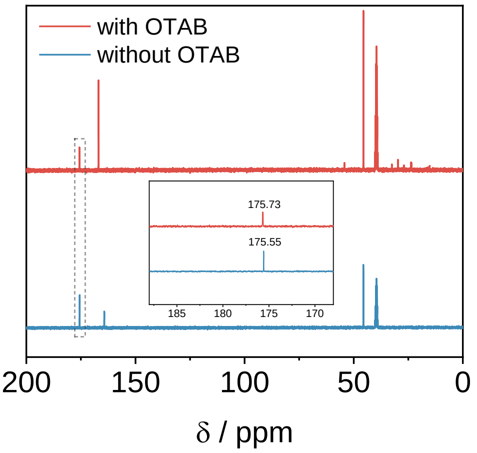

Supplementary Fig. 22 NMR spectra. ^{13}C NMR spectra of MCAA-d_3 electroreduction on LC-Cu without and with OTAB.

Supplementary Note 12 The downfield shift of the carbonyl carbon in MCAA-d_3 indicates that the electrostatic interaction between O^- of MCAA-d_3 and N^+ of OTAB reduces the electron density of O^-, thus enhancing the adsorption of MCAA-d_3 on the electrode surface.[8–9] The peaks at ~160 ppm are assigned to the CO_3^{2-}, and the solvent peak of DMSO-d_6 was referenced to 39.6 ppm.

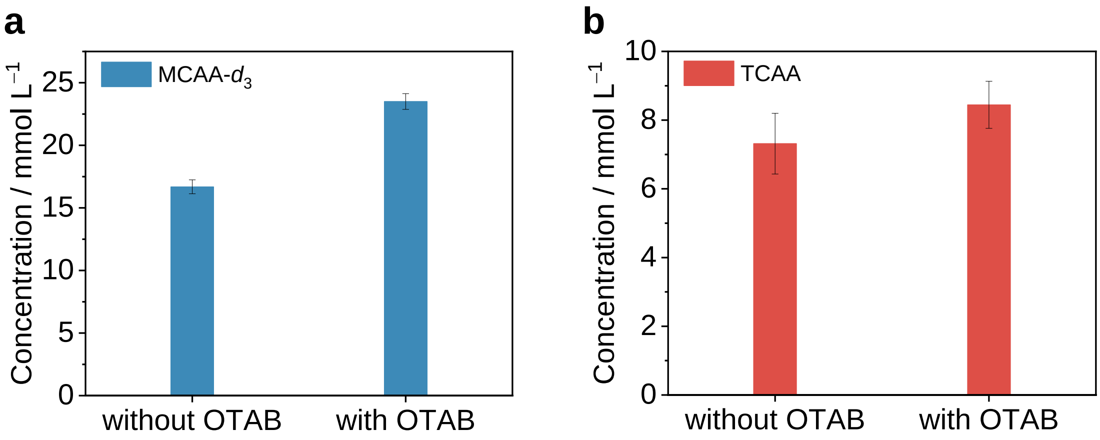

Supplementary Fig. 23 Local concentration measurement around the electrode. Concentration of **a,** MCAA-d_3 and **b,** TCAA surrounding LC-Cu without OTAB and with OTAB.

Supplementary Note 13 The local concentration of MCAA-d_3 around the electrode increases after the adsorption of OTAB, confirming that OTAB can enhance the adsorption of MCAA-d_3 through electrostatic forces. According to the obtained MCAA-d_3 dechlorodeuteration as a first-order reaction, the increase in the local concentration on the electrode surface by OTAB contributes to the acceleration of the first-order kinetic process.[10–11]

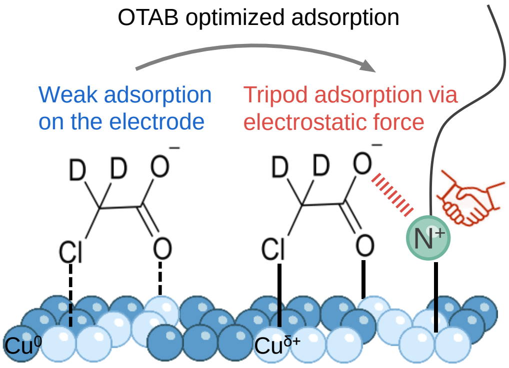

Supplementary Fig. 24 Tripod effect. Schematic illustration patterns of MCAA-d_3 adsorbed on LC-Cu with and without OTAB, respectively.

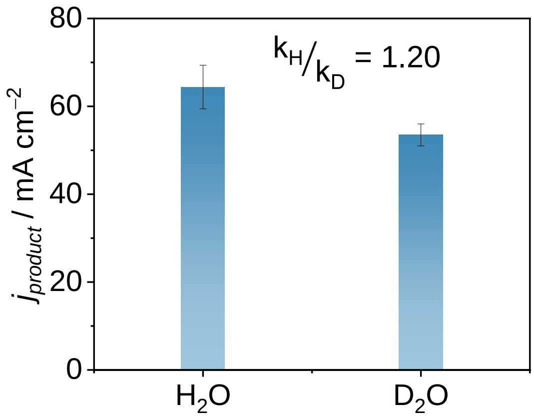

Supplementary Fig. 25 Kinetic isotope effect (KIE) experiments over the LC-Cu cathode. Conditions: 0.5 mmol MCAA-d_3 in 0.5 M K_2CO_3 by using H_2O and D_2O as electrolytes at –0.95 V with a passed charge of 19.297 C.

Supplementary Note 14 The obtained KIE value of 1.20 clearly excluded the possibility of D* generation from D_2O dissociation as the rate-determining step.[12]

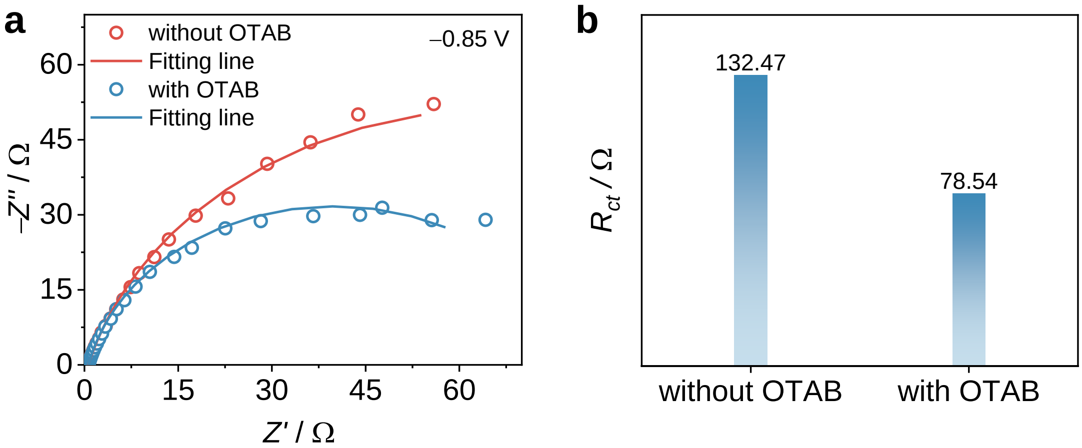

Supplementary Fig. 26 Electrochemical impedance spectroscopy. a, Nyquist plots and **b,** charge transfer resistance of LC-Cu without and with 0.75 mM OTAB at 0.5 M K_2CO_3 containing 0.5 mmol MCAA-d_3 at –0.85 V.

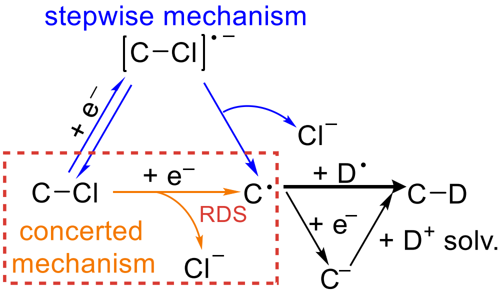

Supplementary Fig. 27 Schematic diagram of two possible mechanisms proposed for the electroreduction of chlorides.

Supplementary Note 15 A stepwise mechanism[13] leads to the generation of the radical anion [C–Cl]$^{\cdot-}$, and the electron is temporarily stored in the C–Cl bond. The concerted mechanism[14] involves electron transfer to the C–Cl bond with concomitant bond cleavage, directly generating the radical C$^{\cdot}$.

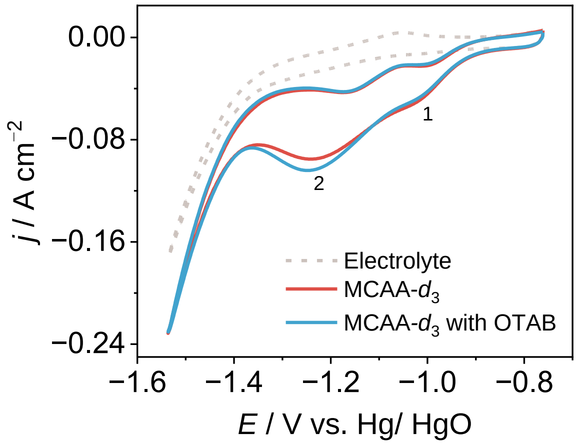

Supplementary Fig. 28 CV measurements. The CV curves of the pure electrolyte, MCAA-d_3 and MCAA-d_3 with OTAB.

Supplementary Note 16 The CV curves of MCAA-d_3 electroreduction indicated that no obvious reduction peak was observed in the pure electrolyte. When MCAA-d_3 was added to the electrolyte, two obvious reduction peaks appeared. The first reduction peak (1) existed as a corresponding reversible oxidation peak, which was probably caused by the adsorption and desorption of MCAA-d_3 on the electrode surface.[15] The second irreversible reduction peak (2) represented electron transfer to the adsorbed MCAA-d_3 process.

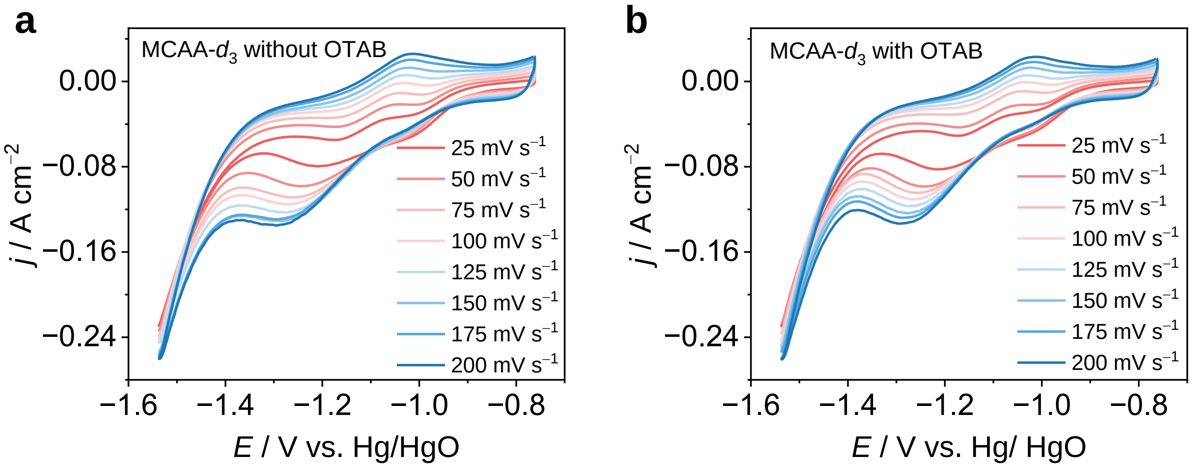

Supplementary Fig. 29 CV measurements. CV curves at different scan rates (25–200 mV s^{-1}) of MCAA-d_3 **a,** without OTAB and **b,** with OTAB.

Supplementary Note 17 The peak current i_p is proportional to $v^{1/2}$, and by plotting the peak potential E_p against v in a linear relationship, the electron transfer coefficient α can be determined.

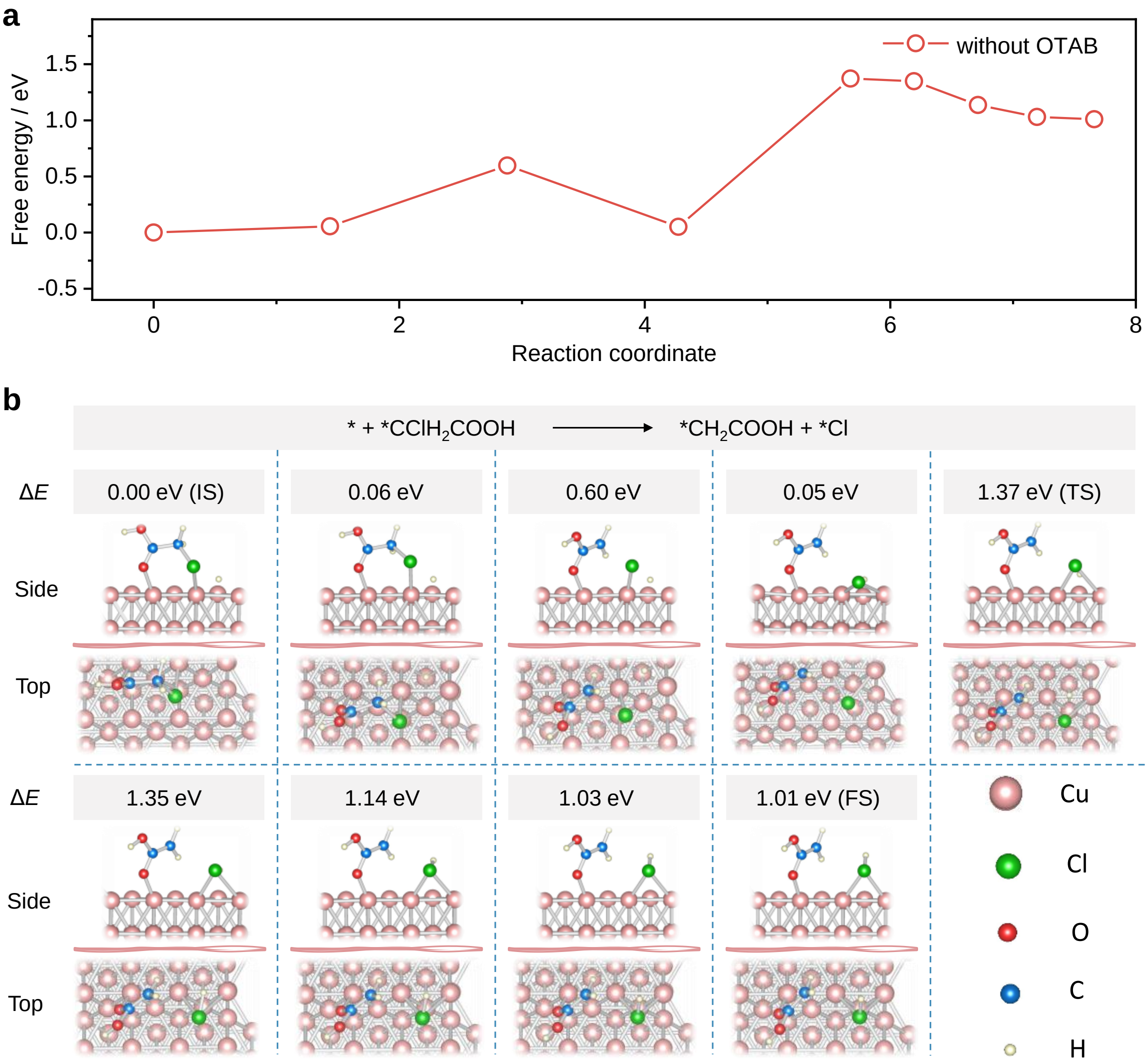

Supplementary Fig. 30 Reaction pathway simulation. a, Energy profiles and **b,** theoretical adsorption models of the transition states (TS) for C–Cl bond dissociation of MCAA without OTAB on the surface of LC-Cu.

Supplementary Note 18 The transition state (TS) searches are performed via the Dimer method in the VTST package. The final force on each atom was < 0.1 eV $Å^{-1}$. The TS search is conducted by using the climbing-image nudged elastic band (CI–NEB) method to generate initial guess geometries, followed by the dimer method to converge to the saddle points.

The adsorption energy of the reaction intermediates can be computed via Eqs. (1–2):

$$\Delta E = E_{*\mathrm{ads}} - (E_{*} + E_{\mathrm{ads}}) \qquad (1)$$

$$\Delta G = \Delta E + \Delta E_{\mathrm{ZPE}} - T\Delta S \tag{2}$$

where ΔE_{ZPE} is the zero-point energy change and ΔS is the entropy change. In this work, the values of ΔE_{ZPE} and ΔS were obtained via vibration frequency calculations.

The energy of the reaction can be calculated via Eqs. (3–14):

$$* + H_2O + e^- \rightarrow *H + OH^- \tag{3}$$

$$3*H + CCl_3COOH \rightarrow 3*H + *CCl_3COOH \tag{4}$$

$$3*H + *CCl_3COOH \rightarrow 2*H + *CCl_2COOH + *HCl \tag{5}$$

$$2*H + *CCl_2COOH + *HCl \rightarrow 2*H + *CCl_2COOH + HCl \tag{6}$$

$$2*H + *CCl_2COOH \rightarrow *H + *CHCl_2COOH \tag{7}$$

$$3*H + *CHCl_2COOH \rightarrow 2*H + *CHClCOOH + *HCl \tag{8}$$

$$2*H + *CHClCOOH + *HCl \rightarrow 2*H + *CHClCOOH + HCl \tag{9}$$

$$2*H + *CHClCOOH \rightarrow *H + *CH_2ClCOOH \tag{10}$$

$$3*H + *CH_2ClCOOH \rightarrow 2*H + *CH_2COOH + *HCl \tag{11}$$

$$2*H + *CH_2COOH + *HCl \rightarrow 2*H + *CH_2COOH + HCl \tag{12}$$

$$2*H + *CH_2COOH \rightarrow *H + *CH_3COOH \tag{13}$$

$$*H + *CH_3COOH \rightarrow *H + CH_3COOH \tag{14}$$

The activation energy for the C−Cl bond dissociation of MCAA on LC-Cu is 1.37 eV, and the final state energy is 1.01 eV, indicating that the C−Cl bond dissociation process is thermodynamically unfavourable.

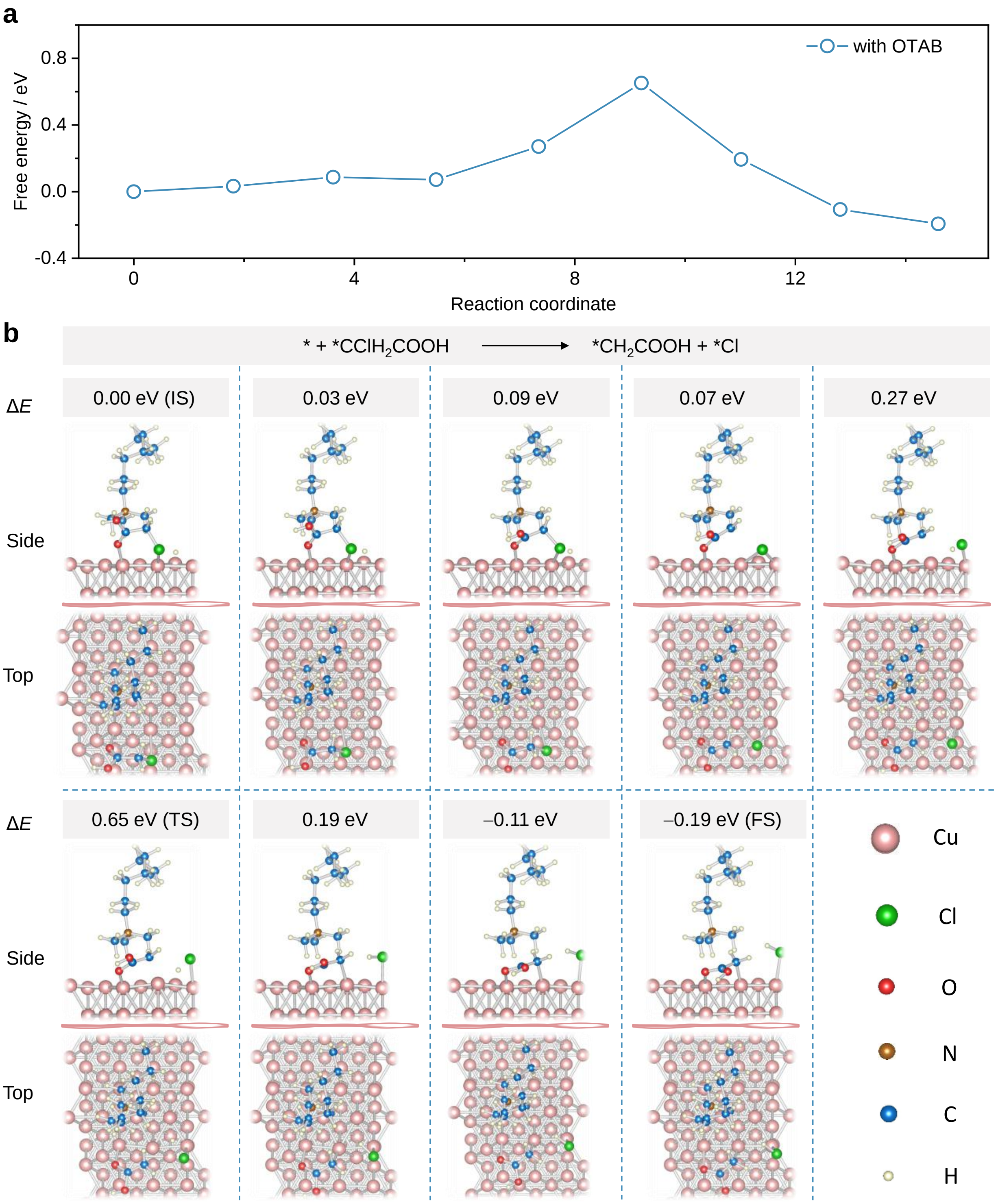

Supplementary Fig. 31 Reaction pathway simulation. a, Energy profiles and **b,** theoretical adsorption models of the transition states (TS) for C–Cl bond dissociation of MCAA with OTAB on the surface of LC-Cu.

Supplementary Note 19 The activation energy for the C–Cl bond dissociation of MCAA on LC-Cu is 0.65 eV after the adsorption of OTAB, and the final state energy is −0.19 eV, indicating that the C−Cl bond dissociation process is thermodynamically favourable. In contrast, the C atom exhibits a sp^2 hybridization state after the removal of a Cl atom in MCAA on LC-Cu, whereas when MCAA removes a Cl atom on LC-Cu with OTAB adsorption, the C atom shows a more stable sp^3 hybridization state, which is more favourable for the cleavage of the C−Cl bond (Supplementary Fig. 30).

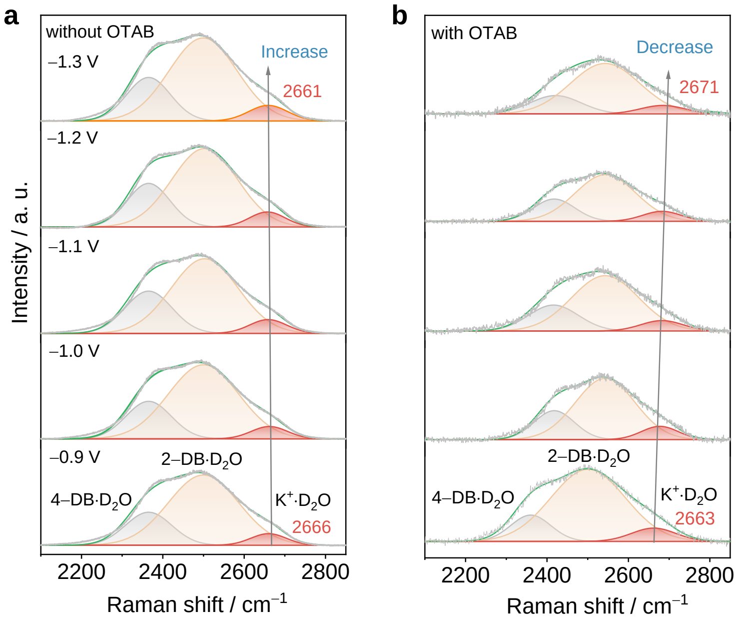

Supplementary Fig. 32 Raman spectra. Potential-dependent in situ Raman spectra of interfacial D_2O on LC-Cu **a,** without OTAB and **b,** with OTAB.

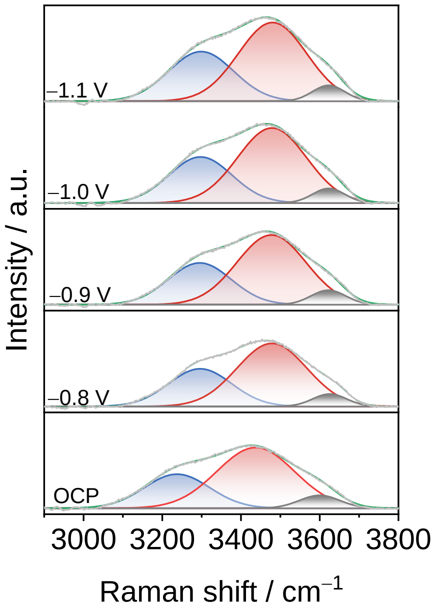

Supplementary Fig. 33 Raman spectra. In situ Raman spectra of interfacial H_2O on the LC-Cu electrode in a 0.5 M K_2CO_3 solution.

Supplementary Note 20 Gaussian fitting of the O–H stretching band can be resolved into three distinct components, corresponding to three types of O–H stretching vibrations. The blue pattern represents 4–coordinated hydrogen-bonded water (4–HB H_2O), the red pattern represents 2–coordinated hydrogen-bonded water (2–HB H_2O), and the grey pattern represents K^+ hydrated water (K^+ H_2O).[16] The stretching vibration peaks of the three types of O–D bonds in D_2O all redshift because the vibration frequency of the O–D bond is lower than that of the O–H bond (Supplementary Fig. 32a, b).[17–18]

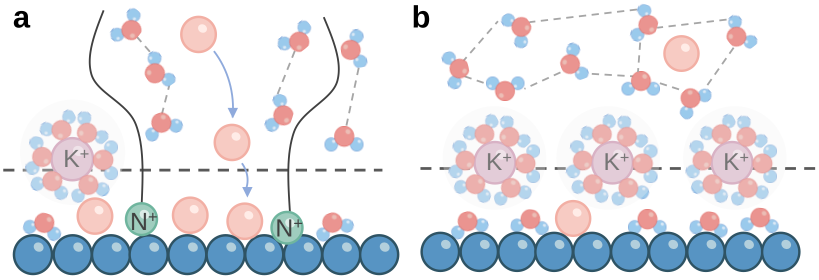

Supplementary Fig. 34 Schematic illustration of the electrode–electrolyte interface. a, with and **b,** without a surfactant. The pink spheres represent the reactants.

Supplementary Note 21 As shown in Supplementary Fig. 34a, the surfactant can disrupt the deuterium-bonding network structure, repel K^+-D_2O and promote the transport of reactants to the electrode surface. However, if the electrode surface is covered with abundant D_2O, the dense deuterium-bonding network structure hinders the migration of reactants to the electrode surface, which is unfavourable for the catalytic reaction (Supplementary Fig. 34b).

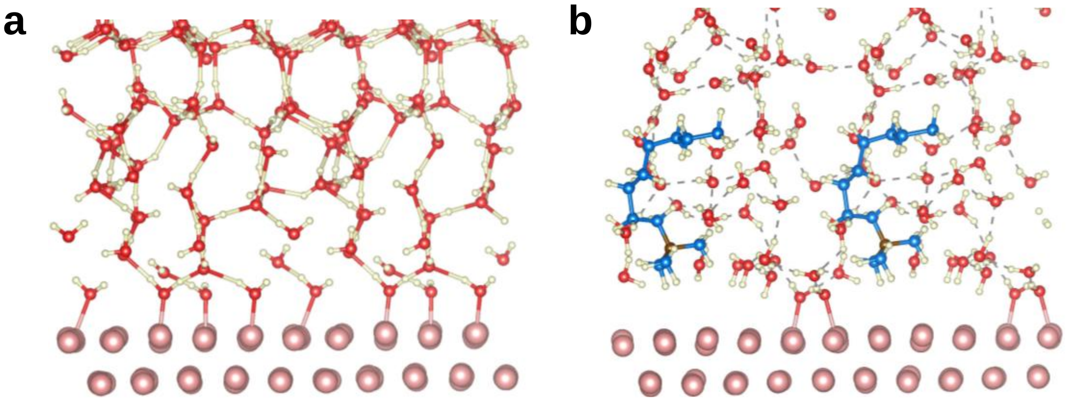

Supplementary Fig. 35 AIMD simulation of interfacial water. AIMD simulation model for aqueous solutions **a,** without and **b,** with OTAB.

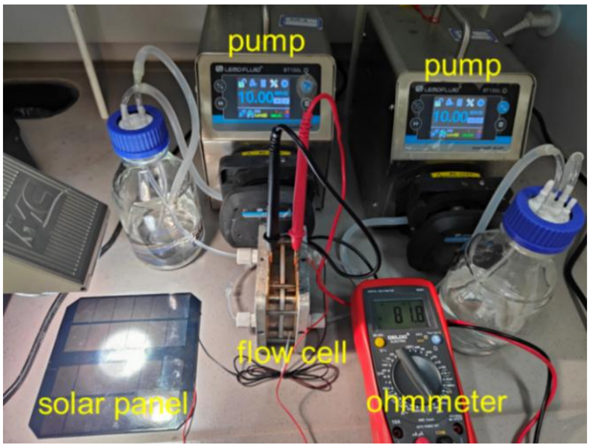

Supplementary Fig. 36 Photograph of the solar-powered electrosynthesis of the AA-d_4 system.

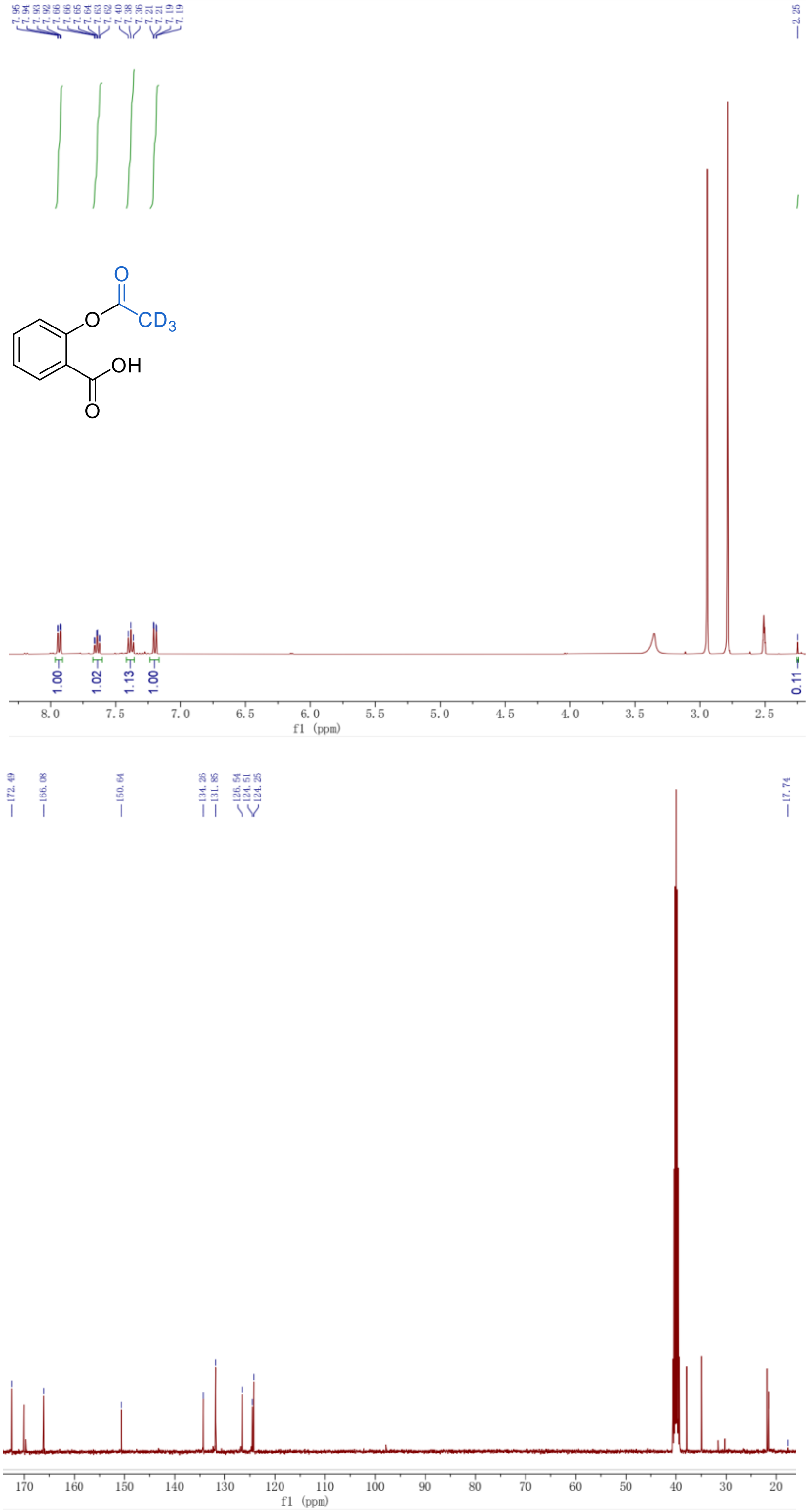

Supplementary Fig. 37 NMR spectra of *aspirin−d*$_3$. ^{1}H NMR (400 MHz, DMSO−*d*$_6$) δ (ppm) 7.93 (dd, *J* = 7.7, 1.7 Hz, 1H), 7.64 (td, *J* = 7.6, 1.7 Hz, 1H), 7.38 (td, *J* = 7.6, 1.2 Hz, 1H), 7.20 (dd, *J* = 8.1, 1.2 Hz, 1H), 2.25 (s, 0H). ^{13}C NMR (101 MHz, DMSO−*d*$_6$) δ (ppm) 172.49, 166.08, 150.65, 134.27, 131.85, 126.54, 124.51, 124.25, 17.74.

Supplementary Note 22 The synthesis method was modified from previously reported methods.[19–20] A total of 2.5 mmol of AA-*d₄* and 800 μL of *N*,*N*–dimethylacetamide were dissolved in 2 mL of dichloromethane (DCM) by stirring at room temperature. The mixture was cooled to 0 ℃, and then 3 mmol of thionyl chloride ($SOCl_2$) was slowly added dropwise, maintaining the reaction at 0 ℃ for 30 minutes. Next, 2 mmol of salicylic acid dissolved in 3 mL of DCM and 2.5 mmol of triethylamine were added, and the mixture was warmed and maintained at 25 ℃ for 6 hours. After completion of the reaction, 6 mL NaCl saturated solution and 6 mL ethyl acetate were added sequentially to the reaction mixture, which was then transferred to a separatory funnel. The aqueous layer was extracted with ethyl acetate (6 mL × 2). The organic layer was subsequently collected, dried over anhydrous Na_2SO_4, and filtered, after which the solvent was removed via rotary evaporation to obtain the crude product. The crude product was further purified by column chromatography (petroleum ether:ethyl acetate:acetic acid = 50:10:1) to obtain the white product. In addition to differences in the reaction solvent, time, and ratio of the column chromatography eluent, the synthesis methods of *paracetamol*-d_3, *celecoxib*-d_3, *dihydroartemisinin*-d_3, *and oseltamivir*-d_3 are similar.

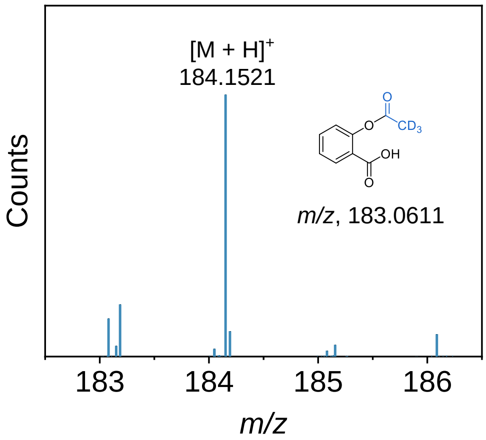

Supplementary Fig. 38 HRMS of *aspirin−d*$_3$. HRMS (ESI-TOF) found 184.1521, theoretical value for $C_9H_5D_3O_4$ *m/z* $[M+H]^+$ 184.0611.

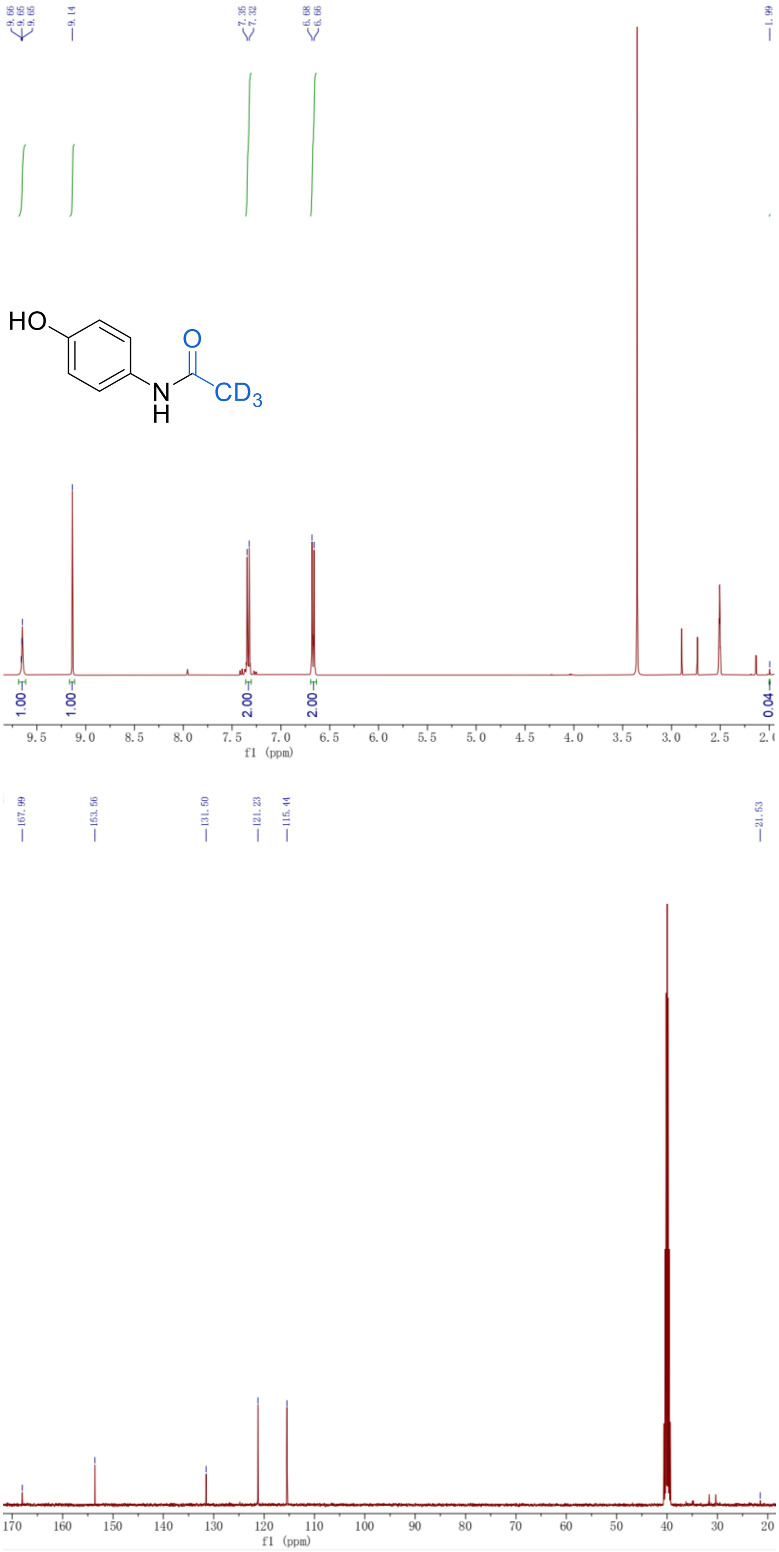

Supplementary Fig. 39 NMR spectra of *paracetamol−d_3*. ^{1}H NMR (400 MHz, DMSO–d_6) δ (ppm) 9.65 (d, J = 2.3 Hz, 1H), 9.14 (s, 1H), 7.36–7.31 (m, 2H), 6.70–6.64 (m, 2H). ^{13}C NMR (101 MHz, DMSO–d_6) δ (ppm) 167.99, 153.56, 131.50, 121.23, 115.44, 21.53.

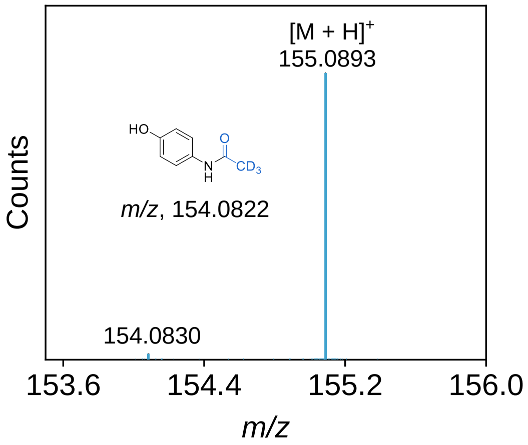

Supplementary Fig. 40 HRMS of *paracetamol-d*$_3$. HRMS (ESI-TOF) found 155.0893, theoretical value for $C_8H_6D_3NO_2$ *m/z* $[M+H]^+$ 155.0822.

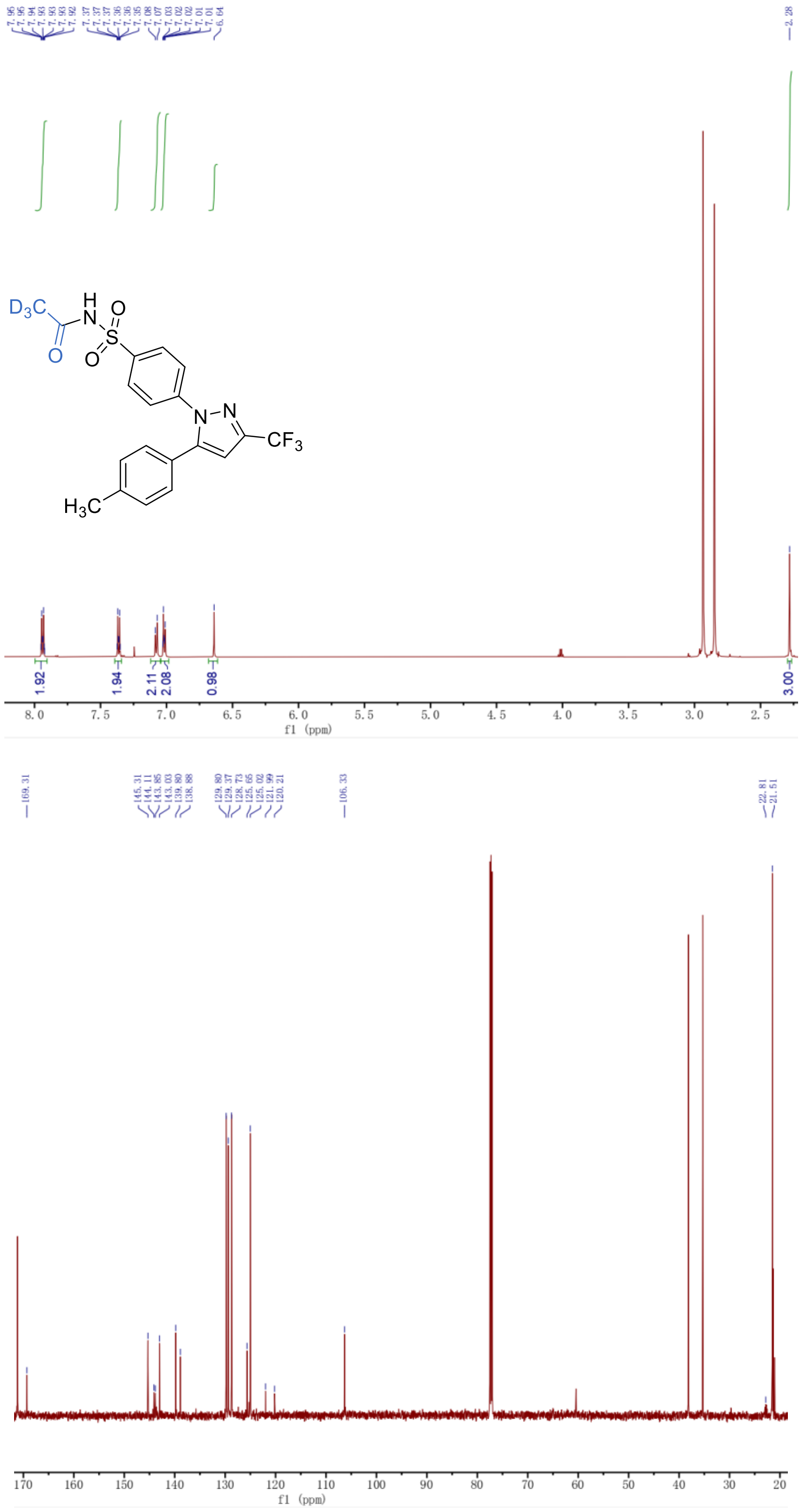

Supplementary Fig. 41 NMR spectra of *celecoxib-d*$_3$. ^{1}H NMR (600 MHz, CDCl$_3$–*d*) δ (ppm) 7.98–7.91 (m, 2H), 7.40–7.34 (m, 2H), 7.08 (d, *J* = 8.0 Hz, 2H), 7.05–6.99 (m, 2H), 6.64 (s, 1H), 2.28 (s, 3H). ^{13}C NMR (151 MHz, CDCl$_3$–*d*) δ (ppm) 169.31, 145.31, 144.11, 143.85, 143.03, 139.80, 138.88, 129.80, 129.37, 128.73, 125.65, 125.02, 121.99, 120.21, 106.34, 22.81, 21.51.

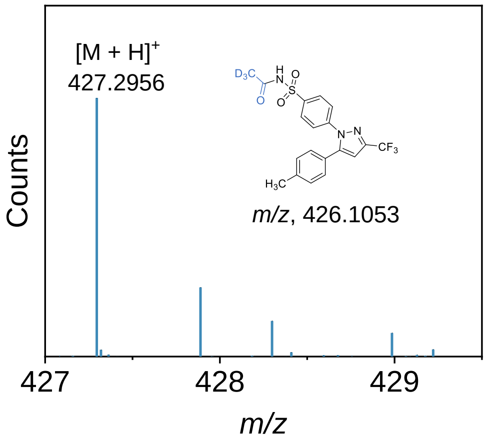

Supplementary Fig. 42 HRMS of *celecoxib-d*$_3$. HRMS (ESI-TOF) found 427.2956, theoretical value for $C_{19}H_{13}D_3F_3N_3O_3S$ *m/z* $[M+H]^+$ 427.1053.

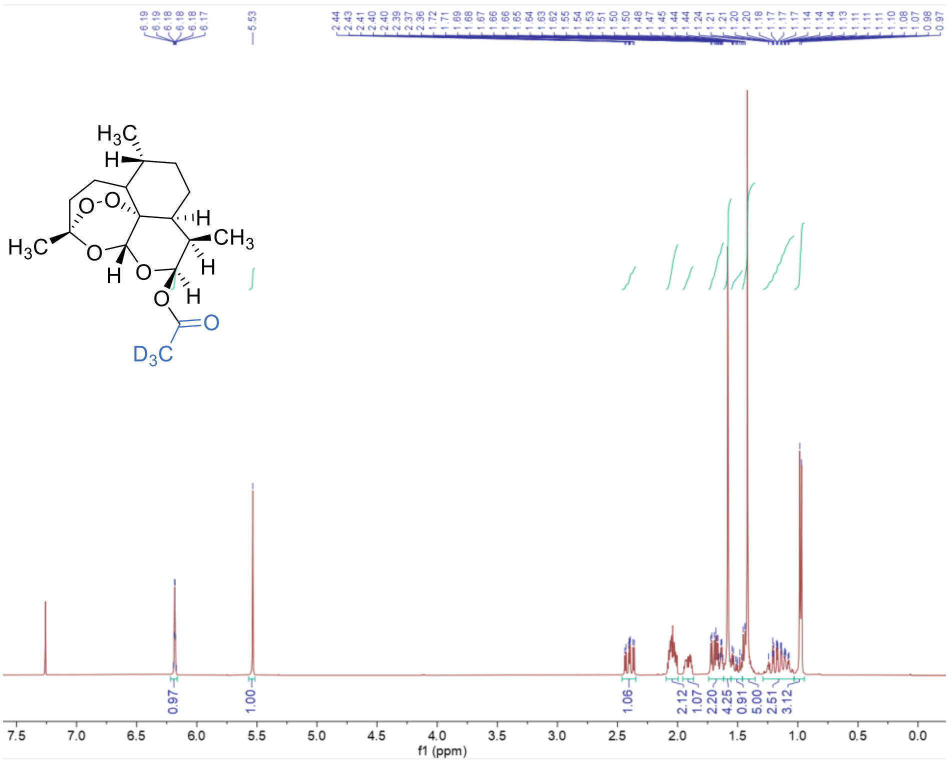

Supplementary Fig. 43 NMR spectra of *dihydroartemisinin-d_3*. ^{1}H NMR (400 MHz, $CDCl_3$–*d*) δ (ppm) 6.12 (q, *J* = 1.5 Hz, 2H), 5.47 (s, 2H), 2.34 (dd, *J* = 4.0, 1.5 Hz, 1H), 2.30 (d, *J* = 4.1 Hz, 1H), 1.66 (s, 1H), 1.61 (dd, *J* = 7.7, 3.8 Hz, 2H), 1.57 (q, *J* = 3.0 Hz, 1H), 1.48 (d, *J* = 4.9 Hz, 1H), 1.40 (d, *J* = 10.7 Hz, 1H), 1.38 (s, 1H), 1.21 – 0.99 (m, 5H), 0.91 (d, *J* = 6.0 Hz, 6H).

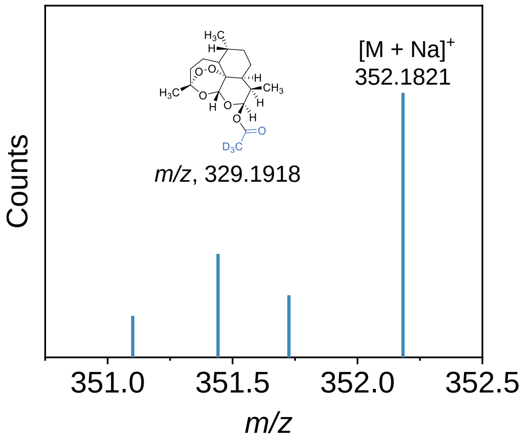

Supplementary Fig. 44 HRMS of *dihydroartemisinin-d*$_3$. HRMS (ESI-TOF) found 352.1821, theoretical value for $C_{17}H_{23}D_3O_6$ *m/z* [M+Na]$^+$ 352.1918.

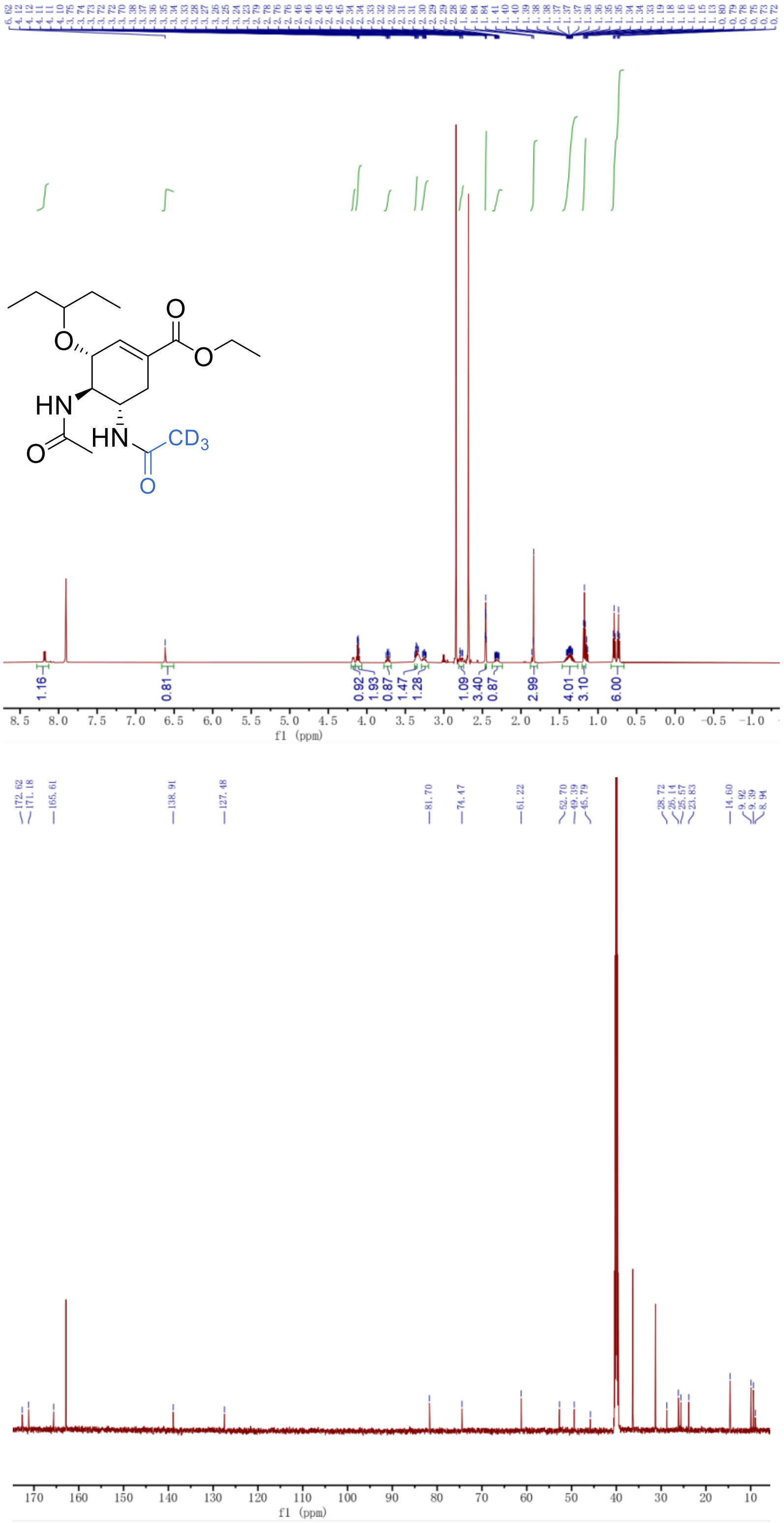

Supplementary Fig. 45 NMR *spectra of oseltamivir-d*$_3$. ^{1}H NMR (600 MHz, DMSO–d_6) δ (ppm) 8.18 (d, J = 8.8 Hz, 1H), 6.66–6.51 (m, 1H), 4.18 (dt, J = 8.9, 2.5 Hz, 1H), 4.12 (qd, J = 7.1, 1.3 Hz, 2H), 3.73 (dt, J = 11.4, 8.8 Hz, 1H), 3.36 (q, J = 5.6 Hz, 1H), 3.25 (td, J = 10.9, 5.5 Hz, 1H), 2.77 (dd, J = 17.2, 5.7 Hz, 1H), 2.31 (ddt, J = 17.0, 10.5, 3.2 Hz, 1H), 1.84 (s, 3H), 1.47–1.26 (m, 4H), 1.18 (t,

J = 7.1 Hz, 3H), 0.83–0.66 (m, 6H). ^{13}C NMR (151 MHz, DMSO-d_6) δ (ppm) 172.62, 171.18, 165.61, 138.91, 127.48, 81.70, 74.47, 61.22, 52.70, 49.39, 45.79, 40.52, 28.72, 26.14, 25.57, 23.83, 14.60, 9.92, 9.39, 8.94.

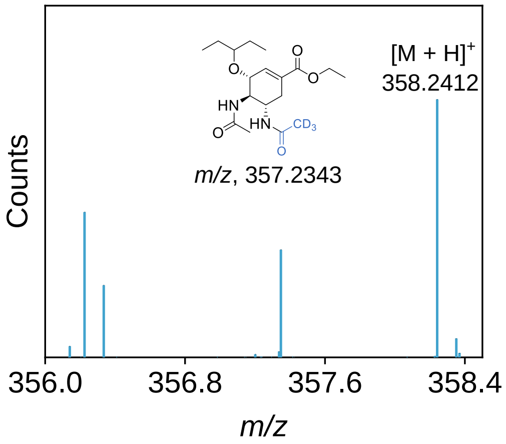

Supplementary Fig. 46 HRMS of *oseltamivir-d*$_3$. HRMS (ESI-TOF) found 358.2412, theoretical value for $C_{18}H_{27}D_3N_2O_5$ *m/z* $[M+H]^+$ 358.2343.

References

1. Li, P., Bi, J., Liu, J., Wang, Y., Kang, X., Sun, X., Zhang, J., Liu, Z., Zhu, Q. & Han, B. p–d orbital hybridization induced by p–block metal–doped Cu promotes the formation of C_{2+} products in ampere–level CO_2 electroreduction. *J. Am. Chem. Soc.* **145**, 4675–4682 (2023).
2. Zhu, Y., Chen, Y., Chen, J., Yin, J., Sun, Z., Zeng, G., Wu, X., Chen, L., Yu, X., Luo, H., Yan, Y., Zhang, H., Zhang, B., Kuai, X., Tang, Y., Xu, J., Yin, W., Qiu, Y., Zhang, Q., Qiao, Y. & Sun, S. G. Lattice engineering on Li_2CO_3–based sacrificial cathode prelithiation agent for improving the energy density of Li–ion battery full–cell. *Adv. Mater.* **36**, 2312159 (2024).
3. Li, Y., Cheng, C., Han, S., Huang, Y., Du, X., Zhang, B. & Yu, Y. Electrocatalytic reduction of low–concentration nitric oxide into ammonia over Ru nanosheets. *ACS Energy Lett.* **7**, 1187–1194 (2022).
4. Ren, Z., Wu, M., Chen, X., Li, W., Li, M., Wang, F., Tian, H., Chen, J., Xie, Y., Mai, J., Li, X., Lu, X., Lu, Y., Zhang, H., Van Tendeloo, G., Zhang, Z. & Han, G. Electrostatic force–driven oxide heteroepitaxy for interface control. *Adv. Mater.* **30**, 1707017 (2018).
5. Ma, L., Yao, H., Zhang, J., Chen, Z., Wang, J., Qiao, J., Wang, S., Bi, Z., Li, Z., Hao, X., Wei, Z., Ma, W. & Hou, J. Morphology control by tuning electrostatic interactions for efficient polythiophene–based all–polymer solar cells. *Chem* **9**, 2518–2529 (2023).
6. Tang, S., Xu, L., Peng, B., Xiong, F., Chen, T., Luo, X., Huang, X., Li, H., Zeng, J., Ma, Z. & Wang, L. L. Ga–doped Pd/CeO_2 model catalysts for CO oxidation reactivity: A density functional theory study. *Appl. Surf. Sci.* **575**, 151655 (2022).
7. Li, W., Liu, C., Gu, C., Choi, J. H., Wang, S. & Jiang, J. Interlayer charge transfer regulates single–atom catalytic activity on electride/graphene 2D heterojunctions. *J. Am. Chem. Soc.* **145**, 4774–4783 (2023).
8. Zhao, D., Zhu, Y., Cheng, W., Xu, G., Wang, Q., Liu, S., Li, J., Chen, C., Yu, H. & Hu, L. A dynamic gel with reversible and tunable topological networks and performances. *Matter* **2**, 390–403 (2020).
9. Sun, Q., Oliveira, N. J., Kwon, S., Tyukhtenko, S., Guo, J. J., Myrthil, N., Lopez, S. A., Kendrick, I., Mukerjee, S., Ma, L., Ehrlich, S. N., Li, J., Goddard, W. A., Yan, Y. & Jia, Q. Understanding hydrogen electrocatalysis by probing the hydrogen–bond network of water at the electrified Pt–solution interface. *Nature Energy* **8**, 859–869 (2023).
10. Zhu, M., Ye, R., Jin, K., Lazouski, N. & Manthiram, K. Elucidating the reactivity and

mechanism of CO_2 electroreduction at highly dispersed cobalt phthalocyanine. *ACS Energy Lett.* **3**, 1381–1386 (2018).

11. Jin, K., Maalouf, J. H., Lazouski, N., Corbin, N., Yang, D. & Manthiram, K. Epoxidation of cyclooctene using water as the oxygen atom source at manganese oxide electrocatalysts. *J. Am. Chem. Soc.* **141**, 6413–6418 (2019).
12. Tan, Q., Li, L., Li, Y., Jiang, Z., Ma, Y., Qu, Y. & Li, J. Tandem electrocatalytic alkyne semihydrogenation over bicomponent catalysts through hydrogen spillover. *Angew. Chem. Int. Ed.* **63**, e202400483 (2024).
13. Corbin, N., Junor, G. P., Ton, T. N., Baker, R. J. & Manthiram, K. Toward improving the selectivity of organic halide electrocarboxylation with mechanistically informed solvent selection. *J. Am. Chem. Soc.* **145**, 1740–1748 (2023).
14. Lou, Y. Y., Fontmorin, J. M., Amrane, A., Fourcade, F. & Geneste, F. Metallic nanoparticles for electrocatalytic reduction of halogenated organic compounds: A review. *Electrochim. Acta* **377**, 138039 (2021).
15. Li, S., Dong, X., Zhao, Y., Mao, J., Chen, W., Chen, A., Song, Y., Li, G., Jiang, Z., Wei, W. & Sun, Y. Chloride ion adsorption enables ampere–level CO_2 electroreduction over silver hollow fiber. *Angew. Chem. Int. Ed.* **61**, e202210432 (2022).
16. Wang, Y. H., Zheng, S., Yang, W. M., Zhou, R. Y., He, Q. F., Radjenovic, P., Dong, J. C., Li, S., Zheng, J., Yang, Z. L., Attard, G., Pan, F., Tian, Z. Q. & Li, J. F. In situ raman spectroscopy reveals the structure and dissociation of interfacial water. *Nature* **600**, 81–85 (2021).
17. Ananthakrishnan, R. Raman spectrum of heavy water. *Nature* **136**, 551–552 (1935).
18. Hu, Q., Ouyang, S., Li, J. & Cao, Z. Raman spectroscopic investigation on pure D_2O/H_2O from 303 to 573 K: Interpretation and implications for water structure. *J. Raman Spectrosc* **48**, 610–617 (2017).
19. Zuo, D., Wang, Q., Liu, L., Huang, T., Szostak, M. & Chen, T. Highly chemoselective transamidation of unactivated tertiary amides by electrophilic N–C(O) activation by amide–to–acyl iodide re–routing. *Angew. Chem. Int. Ed.* **61**, e202202794 (2022).
20. Prasad, H. S.; Srinivasa, G. R.; Channe Gowda, D. Convenient, cost–effective, and mild method for the N–acetylation of anilines and secondary amines. *Synthetic Commun.* **35**, 1189–1195 (2005).